Onboard Integrated Battery Charger for EVs Using an Asymmetrical Nine-Phase Machine

Ivan Subotic, *Student Member, IEEE*, Nandor Bodo, Emil Levi, *Fellow, IEEE*, and Martin Jones

***Abstract*—This paper considers an integrated onboard charger for electric vehicles that incorporates an asymmetrical nine-phase machine and an inverter into the charging process. The charging is from three-phase mains, and it employs exclusively the power electronic components that already exist on board the vehicle and that are mandatory for the propulsion. No new elements are introduced. Moreover, the charging is achieved without any hardware reconfiguration since the existing elements and their connections are not altered during the transfer from propulsion to the charging mode. Instead, the operating principle is based on additional degrees of freedom that exist in nine-phase machines. These degrees of freedom are employed to avoid electromagnetic torque production in the machine during the charging process, although currents flow through its stator windings. The configuration operates with a unity power factor and is capable of vehicle to grid (V2G) operation as well. A detailed theoretical analysis is given, and the control for the charging/V2G and propulsion modes is discussed. Theoretical analysis is validated by experiments for charging, V2G, and propulsion operating regimes.**

***Index Terms*—Battery chargers, electric vehicles (EVs), integrated onboard chargers, multiphase machines.**

I. Introduction

ONBOARD chargers are a valuable part of electric vehicles (EVs) as they liberate drivers from the dependence on fast dc charging stations. At present, it is common that chargers for EVs are made as separate units when they are placed on board. Compared to a vehicle without an onboard charger, these units have a negative impact on the cost, weight, and spare space in the vehicle. However, power electronic components that form a typical onboard charger do not differ from the elements that already exist on board and that are required for propulsion. This fact is the origin of the three-decade-old idea [1] that existing power electronic components can be integrated into the charging process. Many proposals for integration [2] have been reported since.

The study performed in [3] shows that the vast majority of EVs have a propulsion motor of either induction or permanent-magnet type. Although several integrated single-phase solutions have been proposed for these types of machines, they are only applicable for slow charging due to the limitations of a single-phase grid. In order to achieve a fast charging, either a dc charging station or a three-phase ac grid has to be employed. For the former option, the driver has to consider the charging station distribution and to plan the route accordingly. Unlike dc charging stations, a three-phase grid is widely available. Nevertheless, at present, only few configurations allow fast integrated charging incorporating an induction or permanent-magnet motor [4]–[11]. Moreover, some of them require a mechanically locked rotor as there is a torque production in the machine during the charging process. This leads to numerous problems with regard to efficiency, increased wear, and audible noise. Only four of the solutions have the advantage of torque-free three-phase charging [8]–[11].

In [8], a three-phase machine in an open-winding configuration, supplied from a triple H-bridge inverter, is considered for the integration into the charging process. In the charging mode, the three-phase grid is directly connected to the midpoints of each of the three machine's stator phase windings. The charging process is controlled in such a manner that the same currents flow through the two half-windings of each phase. As the half windings are in spatial opposition, the winding does not produce a field in the rotor. Since standard three-phase machines do not have access to their winding midpoints, the machine has to be custom-made—in essence, it has to be a symmetrical six-phase machine. The topology has a great advantage that it does not require any hardware reconfiguration between the propulsion and the charging mode of operation. The solution is currently being considered for use in future EVs by Valeo [12].

The first fast integrated charger that found its way into commercial EVs is the one used in Renault ZOE [9]. Its 43-kW "Chameleon" charger can charge 80% of the battery capacity in 30 min. The inverter and synchronous motor with excitation winding, which are used for propulsion, are incorporated into the charging process. However, the charger also requires a junction box which is a nonintegrated element. Its function is to manage the charging process, to convert the alternating current into direct current, and to communicate with the charging station. The charging process is without a torque production in the machine, but an additional power electronic converter is required.

A configuration incorporating an asymmetrical six-phase machine is considered in [10]. It also operates without torque production and utilizes the principle of phase transposition [13]. Hardware reconfiguration is required.

Manuscript received March 10, 2014; revised April 29, 2014 and June 11, 2014; accepted July 14, 2014. Date of publication August 1, 2014; date of current version April 8, 2015. This work was supported by the Engineering and Physical Sciences Research Council, U.K., under the Vehicle Electrical Systems Integration project (EP/I038543/1).

The authors are with the School of Engineering, Technology and Maritime Operations, Liverpool John Moores University, Liverpool L3 3AF, U.K. (e-mail: i.subotic@2011.ljmu.ac.uk; n.bodo@2009.ljmu.ac.uk; e.levi@ljmu.ac.uk; m.jones2@ljmu.ac.uk).

Color versions of one or more of the figures in this paper are available online at http://ieeexplore.ieee.org.

Digital Object Identifier 10.1109/TIE.2014.2345341

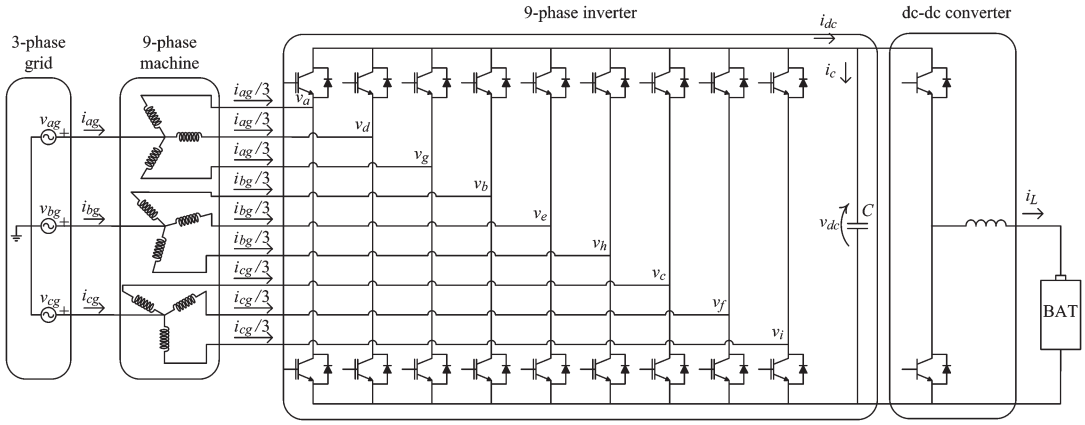

Fig. 1. Topology of the nine-phase fast integrated onboard battery charger.

A topology that does not require any hardware reconfiguration between the operating modes was introduced in [11] at a basic theoretical level. It integrates a nine-phase machine with three isolated neutral points into the charging process. In the charging mode, the three-phase grid connections are directly attached to the three isolated neutral points of the machine. The configuration is controlled in such a way that the same currents flow through all windings belonging to the same three-phase set so that the field is cancelled within the set itself. The control in [11] was based on only the grid current fundamental control in the charging mode, the propulsion mode was treated only at a conceptual level, the vehicle to grid (V2G) mode was not addressed at all, and theory was underpinned by simulation results only.

The same topology is considered here. The work in [11] is advanced by providing a detailed description of an improved control system for the charging mode that includes low-order current harmonic control. The operation is also extended to the V2G mode. Next, control for the propulsion mode is fully developed as well, including current control in all the relevant planes of the nine-phase system. Last but not least, the concept is fully verified experimentally, by providing test results for the charging, V2G, and propulsion modes of operation.

This paper is organized as follows. In Section II, a theoretical analysis of the charging process incorporating an asymmetrical nine-phase machine is given. Complete control algorithms for the charging, V2G, and propulsion modes are presented in Section III. Experimental results for the charging, V2G, and propulsion modes are given in Section IV. Section V concludes this paper.

II. Theoretical Analysis

The investigated topology for the charging/V2G mode is shown in Fig. 1. As can be seen, grid connections are directly attached to the three isolated neutral points of the machine. By simultaneous switching of semiconductors connected to the same grid phase, it is assured that the grid phase current is equally distributed through the three machines' phases that are connected to any particular grid phase. These three phase windings are mutually shifted by 120° so that they do not produce a resultant field when the same currents flow through them.

When the charging/V2G operation is completed, the grid is disconnected, and the topology becomes a regular nine-phase machine with three isolated neutral points. The configuration is now ready for propulsion without any hardware reconfiguration. In the propulsion mode, the system has an advantageous feature, namely, a high degree of fault tolerance, which is increasingly demanded from EVs ("limp home" mode). This is so due to the existence of additional degrees of freedom in multiphase machines (there is a total of six in the propulsion mode, while a three-phase machine has only two).

In order to analyze the machine's behavior during the charging process, a decoupling transformation matrix is required. Although the machine in the propulsion mode has three isolated neutral points, in charging/V2G modes, the neutral points are connected through the grid so that the currents can flow between them. Thus, the decoupling transformation matrix for an asymmetrical nine-phase system with a single neutral point [14] is required to describe the charging/V2G process. Decoupling transformation matrices are given for both cases in the Appendix.

Transformation for charging mode (A.1) can be described using 2-D space vectors as (symbol f denotes the current or voltage, indices α and β denote the flux/torque-producing planes, and indices x and y stand for the non-flux/torque-producing plane)

$$\begin{aligned}
\underline{f}_{\alpha\beta} &= \sqrt{2/9}\,(f_a + \underline{a} f_b + \underline{a}^2 f_c + \underline{a}^6 f_d + \underline{a}^7 f_e \\
&\quad + \underline{a}^8 f_f + \underline{a}^{12} f_g + \underline{a}^{13} f_h + \underline{a}^{14} f_i) \\
\underline{f}_{x1y1} &= \sqrt{2/9}\,(f_a + \underline{a}^3 f_b + \underline{a}^6 f_c + \underline{a}^0 f_d + \underline{a}^3 f_e \\
&\quad + \underline{a}^6 f_f + \underline{a}^0 f_g + \underline{a}^3 f_h + \underline{a}^6 f_i) \\
\underline{f}_{x2y2} &= \sqrt{2/9}\,(f_a + \underline{a}^5 f_b + \underline{a}^{10} f_c + \underline{a}^{12} f_d + \underline{a}^{17} f_e \\
&\quad + \underline{a}^4 f_f + \underline{a}^6 f_g + \underline{a}^{11} f_h + \underline{a}^{16} f_i) \\
\underline{f}_{x3y3} &= \sqrt{2/9}\,(f_a + \underline{a}^7 f_b + \underline{a}^{14} f_c + \underline{a}^6 f_d + \underline{a}^{13} f_e \\
&\quad + \underline{a}^2 f_f + \underline{a}^{12} f_g + \underline{a} f_h + \underline{a}^8 f_i) \\
f_0 &= \sqrt{1/9}\,(f_a - f_b + f_c + f_d - f_e + f_f + f_g - f_h + f_i) \quad (1)
\end{aligned}$$

where $\underline{a} = \exp(j\alpha) = \cos\alpha + j\sin\alpha$ and $\alpha = \pi/9$.

According to Fig. 1, the correlation between machine phase currents and grid currents is given with

$$i_a = i_d = i_g = i_{ag}/3 \quad i_b = i_e = i_h = i_{bg}/3 \quad i_c = i_f = i_i = i_{cg}/3. \quad (2)$$

A. Three-Phase Charging

For the charging process, the three-phase grid currents are given with

$$i_{kg} = \sqrt{2} I \cos(\omega t - l2\pi/3), \quad l = 0, 1, 2; \quad k = a, b, c. \quad (3)$$

The substitution of (2) and (3) into (1) gives the following space vectors:

$$\underline{i}_{\alpha\beta} = 0 \quad \underline{i}_{x2y2} = 0 \quad \underline{i}_{x3y3} = 0$$

$$\underline{i}_{x1y1} = I\left\{(2/3)\cos(\omega t) + (1/\sqrt{3})\sin(\omega t) - j(1/\sqrt{3})\cos(\omega t)\right\} \quad (4)$$

while the zero-sequence component has the value of

$$i_0 = -(\sqrt{8}/3) I \cos(\omega t - 2\pi/3). \quad (5)$$

As is obvious from (4) and (5), the charging process does not utilize the $\alpha - \beta$ plane, and hence, the torque is not produced.

The active $x_1 - y_1$ plane currents are smaller in magnitude since they are complemented with the zero-sequence current of (5) to produce the overall phase currents.

B. Three-Phase V2G Mode

In V2G operation, the three-phase grid currents have the opposite sign and are given with

$$i_{kg} = -\sqrt{2} I \cos(\omega t - l2\pi/3), \quad l = 0, 1, 2; \quad k = a, b, c. \quad (6)$$

Using (6) in conjunction with (2) and (1), the following space vectors are obtained:

$$\underline{i}_{\alpha\beta} = 0 \quad \underline{i}_{x2y2} = \quad \underline{i}_{x3y3} = 0$$

$$\underline{i}_{x1y1} = -I\left\{(2/3)\cos(\omega t) + (1/\sqrt{3})\sin(\omega t) - j(1/\sqrt{3})\cos(\omega t)\right\}. \quad (7)$$

The zero-sequence component is now governed with

$$i_0 = (\sqrt{8}/3) I \cos(\omega t - 2\pi/3). \quad (8)$$

The $\alpha - \beta$ plane is again left without excitation. Presented theoretical derivations confirm that asymmetrical nine-phase machines can be used both for charging and V2G purposes without the generation of a rotating field or torque.

III. Control Algorithm

A. Three-Phase Charging/V2G Modes

Theoretical analysis of Section II implies that sets of three three-phase windings of the asymmetrical nine-phase machine will behave as simple resistive–inductive passive components during the charging/V2G process since the $\alpha - \beta$ plane is left without excitation. The equivalent impedance is composed of the stator leakage inductance and stator resistance [15]; thus,

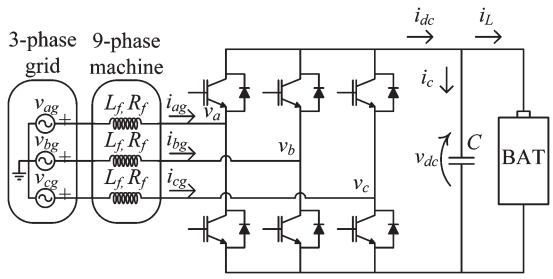

Fig. 2. Equivalent charging/V2G scheme (without a dc–dc converter).

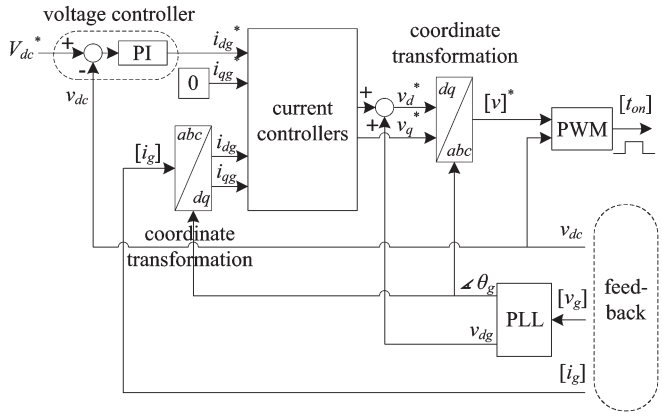

Fig. 3. Control algorithm for the three-phase charging mode.

the equivalent charging/V2G configuration can be represented with Fig. 2, which is a standard three-phase voltage source rectifier.

It is important to emphasize here that, in what follows, it is assumed that all the phases of any of the three three-phase windings are regarded as identical so that they are characterized with the same impedance to current flow and hence enable equal splitting of one grid phase current into the three individual machine's phase currents. As will be shown by means of experimental results, this assumption is satisfied for the machine used in the testing. However, if there are asymmetries in a machine, equal current sharing cannot be ensured in this manner, and the problem of the rectifier/inverter control in charging/V2G modes cannot be approached from the point of view of a three-phase system current control and three-phase pulse width modulation (PWM). Instead, one would have to deal with current control and PWM in terms of a nine-phase system to ensure that asymmetries are correctly compensated and the current equally shared between three phases of each three-phase winding.

In order to achieve unity power factor operation, the configuration is operated using grid voltage-oriented control. The control algorithm is depicted in Fig. 3, and it requires measurements of the dc-bus voltage, grid voltages, and grid currents.

The process starts with obtaining the grid position from the phase-locked loop (PLL), shown in Fig. 4. The resonant filter filters the grid voltage without causing a phase delay. As shown in [16], the PLL of Fig. 4 has a superior performance for a distorted grid voltage, compared to a standard PLL. It is capable of obtaining the position of a single-phase grid as well, which is a requirement in the case of a single-phase charging.

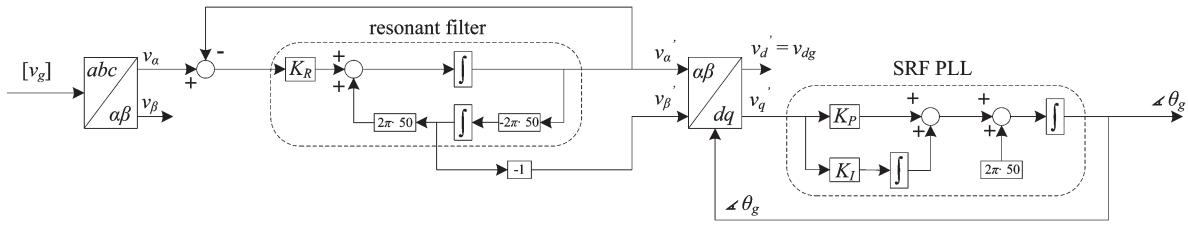

Fig. 4. PLL algorithm (SRF stands for synchronous reference frame).

The obtained information on grid position is used to transform the grid currents into the reference frame that is grid voltage oriented. It is achieved in this way that the grid current component, which is in phase with the grid voltage, is separated and appears as a dc quantity. If the charging process utilizes only this component (i_{dg}), the unity power factor operation during charging will result. The current component that is out of phase with the grid voltage (i_{qg}) should be controlled to zero.

The most conventional way of battery charging is the constant current (CC)–constant voltage (CV) method [17]. It charges the battery with a constant (maximum allowed) current until the battery voltage reaches a certain cutoff level. The charging then continues at a CV until the current drops below 10% of its maximum. For the CC mode, the reference for the component i_{dg} is the desired value of the grid current d-axis component. For the CV mode, the dc-bus voltage is the input reference to the system. As the i_{dg} component is directly proportional to the voltage drop on the battery's internal resistance, its reference can be obtained by a proportional-integral (PI) voltage controller, which is shown as the outer control loop in Fig. 3.

As transient performance in this mode is not of particular interest, a simple carrier-based PWM with zero-sequence injection is used as the modulation strategy.

The current controller algorithm of Fig. 3 is given in more detail in Fig. 5. As grid current components i_{dg} and i_{qg} are dc quantities, they are controlled to their references with standard PI controllers. The decoupling network is necessary to eliminate the coupling effect that exists between the components. It can be seen in Fig. 5 that reference currents are subtracted from measured currents, which is opposite compared to the standard drive current controllers. The reason for this is that, when the amplitude of the inverter voltage increases, the voltage across the filter (i.e., charging current) decreases and vice versa.

Due to the inverter dead-time effect and the potential grid voltage distortion, the grid currents have low-order odd harmonics, primarily the 5th, 7th, 11th, and 13th. In the synchronous dq reference frame, the 7th and the 13th harmonic, which rotate in the synchronous direction, appear as the 6th and the 12th harmonic. The 5th and 11th harmonics rotate in anti-synchronous direction, and in the synchronous reference frame, they are seen as the -6th and -12th harmonics. Since they are ac quantities in this reference frame, the PI controller of Fig. 5 cannot suppress them; additional controllers are thus necessary.

One way of controlling these harmonics would be to utilize four PI controllers in each axis in reference frames that rotate at 6, -6, 12, and -12 times the speed of the synchronous reference frame. However, this would be computationally very

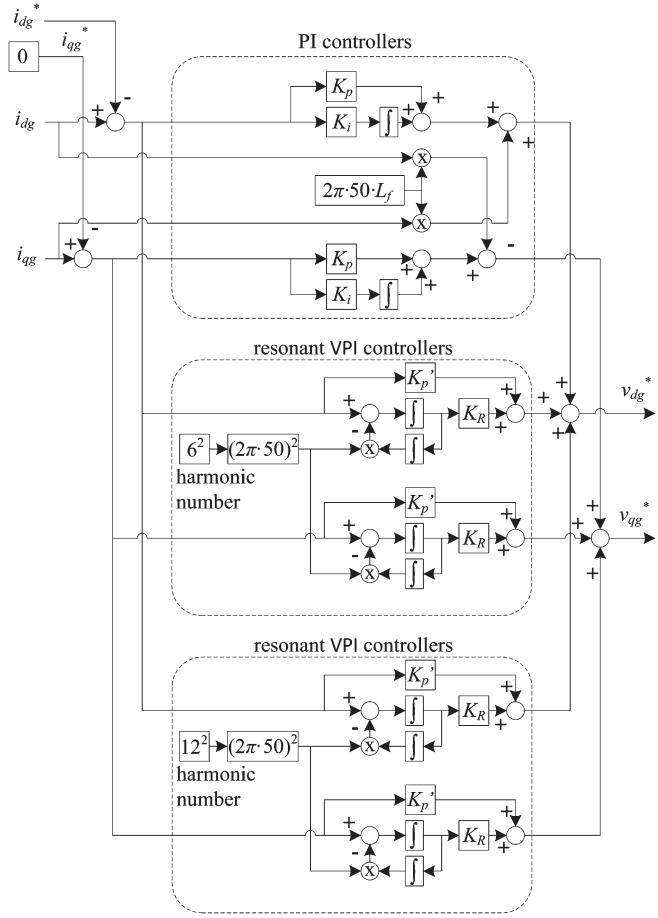

Fig. 5. Current controllers for the three-phase charging/V2G mode.

demanding. Moreover, the cross-coupling between the axes cannot be eliminated for both 6th and -6th harmonics (the same is valid for the 12th and -12th as well) as they would cancel each other's effect, as shown in [18]. A better solution is therefore to employ resonant controllers that are tuned at 6th and 12th harmonic frequencies. As resonant controllers are capable of controlling harmonics rotating in both positive and negative directions of the resonant frequency at the same time, two resonant controllers in each of the two axes can control all four harmonics (see Fig. 5). Vector proportional-integral (VPI) controllers [19] are utilized since standard proportional-resonant controllers cannot provide decoupling for both positive and negative sequence harmonics simultaneously [18]. The presented control algorithm for charging can be applied without any modifications for the V2G mode. It is only necessary to reverse the sign of the reference for the grid current d-axis component.

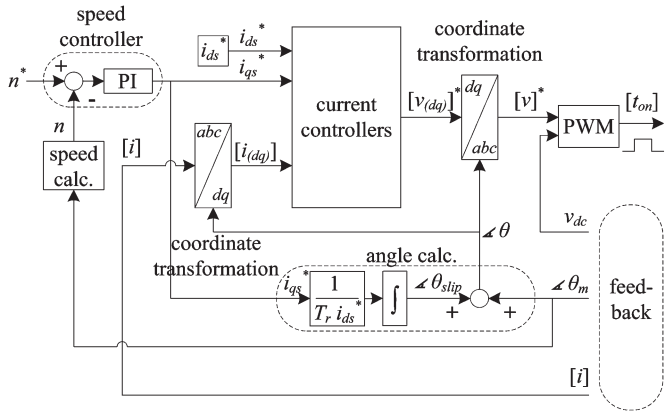

Fig. 6. Control algorithm for the propulsion mode.

B. Propulsion

In the propulsion mode, the drive is operated according to the field-oriented-control principles for multiphase machines [20]. The control algorithm for the propulsion mode is given in Fig. 6, and it can be seen that, in the basic form, it is the same as for three-phase machines, except that the coordinate transformation is governed by (A.2). However, an asymmetrical nine-phase machine with three isolated neutral points has four additional current components that also have to be controlled, and hence, the difference appears in the block "current controllers" in Fig. 6. These current components can be represented in two additional planes, $x_1 - y_1$ and $x_2 - y_2$. The decoupling transformation matrix is now different [see Appendix A, (A.2)]. Hence,

$$\begin{aligned}
\underline{f}_{\alpha\beta} &= \sqrt{2/9}\,(f_a + \underline{a} f_b + \underline{a}^2 f_c + \underline{a}^6 f_d + \underline{a}^7 f_e \\
&\quad + \underline{a}^8 f_f + \underline{a}^{12} f_g + \underline{a}^{13} f_h + \underline{a}^{14} f_i) \\
\underline{f}_{x1y1} &= \sqrt{2/9}\,(f_a + \underline{a}^5 f_b + \underline{a}^{10} f_c + \underline{a}^{12} f_d + \underline{a}^{17} f_e \\
&\quad + \underline{a}^4 f_f + \underline{a}^6 f_g + \underline{a}^{11} f_h + \underline{a}^{16} f_i) \\
\underline{f}_{x2y2} &= \sqrt{2/9}\,(f_a + \underline{a}^7 f_b + \underline{a}^{14} f_c + \underline{a}^6 f_d + \underline{a}^{13} f_e \\
&\quad + \underline{a}^2 f_f + \underline{a}^{12} f_g + \underline{a} f_h + \underline{a}^8 f_i) \\
f_{0_1} &= \sqrt{1/3}\,(f_a + f_d + f_g) \\
f_{0_2} &= \sqrt{1/3}\,(f_b + f_e + f_h) \\
f_{0_3} &= \sqrt{1/3}\,(f_c + f_f + f_i). \qquad (9)
\end{aligned}$$

It can be shown that low-order odd harmonics map in the additional planes according to the following rule: The 5th and -13th map into the second $(x_1 - y_1)$ plane, and the 7th and -11th map into the third $(x_2 - y_2)$ plane. Note the important difference regarding the direction of rotation of the harmonics in the nine-phase system and the three-phase system.

The use of resonant controllers for harmonic compensation in multiphase machines has been successfully demonstrated in [21] for a six-phase machine. In the asymmetrical nine-phase case, in order to control the 5th and -13th harmonics using a resonant controller, it has to be placed in a reference frame that rotates at a speed that is four times the synchronous speed and

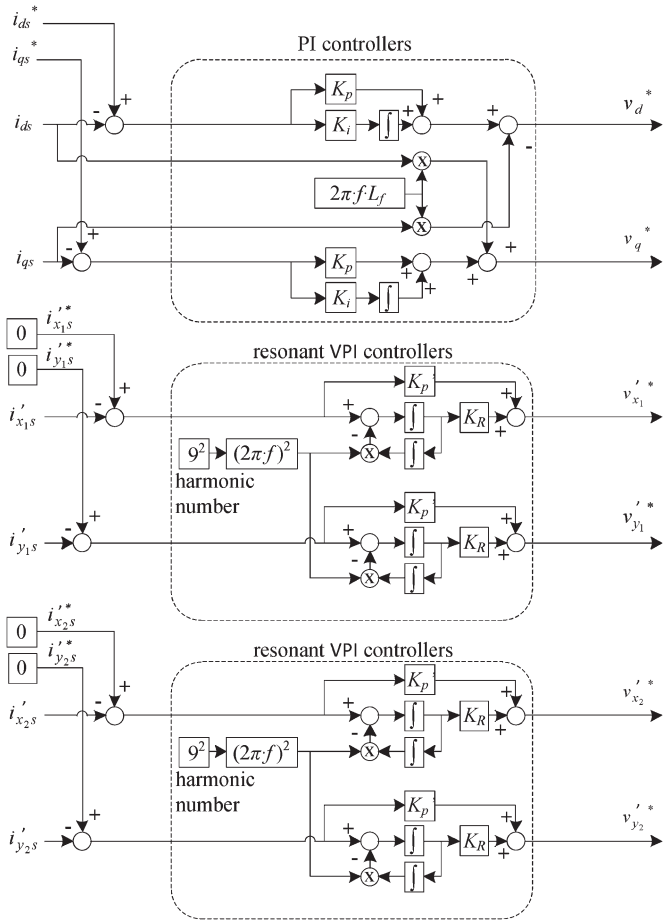

Fig. 7. Current controllers for the propulsion mode.

that rotates in the opposite (antisynchronous) direction. In that reference frame, the 5th and the -13th harmonic will be seen as the 9th and -9th, respectively. Hence, both can be controlled with a single VPI controller in the same manner in which it was done for the charging/V2G mode. Similarly, the harmonics of the third plane can be controlled in the reference frame that rotates at twice the synchronous speed in the opposite direction. Then, the 7th and -11th harmonics will be seen as the 9th and -9th, and again, they can be controlled with the VPI controller with the resonant frequency nine times the synchronous one. The complete current control algorithm for the propulsion mode is given in Fig. 7.

It should be noted that the $x - y$ current and voltage axis components in Fig. 7 are those obtained after the application of (A.2) and subsequent rotational transformation (hence the superscript $'$). In particular, $x_1' - y_1'$ components are in the reference frame that rotates at four times the synchronous speed in antisynchronous direction, while $x_2' - y_2'$ components are in the reference frame that rotates at twice the synchronous speed, also in antisynchronous direction.

The modulation strategy is again standard carrier-based PWM with zero-sequence injection. However, since the machine has three isolated sets of windings, zero-sequence injection can be applied to each set separately. This improves the dc-bus utilization which is, in essence, equal to the one of three-phase machines.

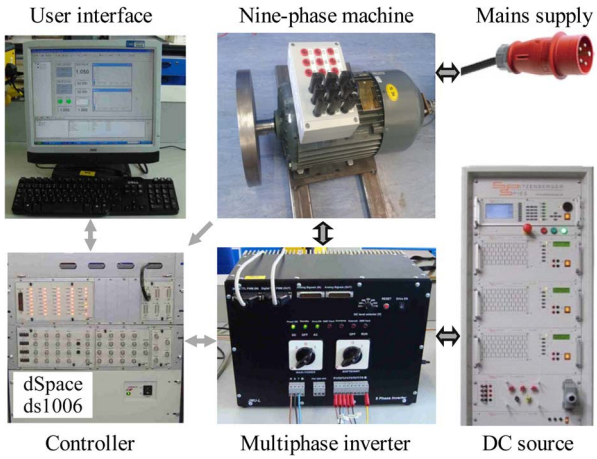

Fig. 8. Experimental setup for charging, V2G, and propulsion modes.

IV. Experimental Results

In order to verify the presented theoretical concepts, experimental results are obtained for the charging, V2G, and propulsion modes of operation using the asymmetrical nine-phase machine. The experimental setup, which corresponds to the schematic of Fig. 1, is shown in Fig. 8. The three-phase grid is connected to the nine-phase machine's neutral points. The machine is connected to two eight-phase inverters (only one is shown in Fig. 8), one of which provides voltages to six machine phases and the other to the three remaining phases. The dc buses of the two inverters are connected, and they are supplied by a four-quadrant amplifier "Spitzenberger & Spies" (data in Appendix B), labeled as "DC source" in Fig. 8, which emulates the battery. A dc–dc converter of Fig. 1 is omitted since its presence or absence is irrelevant from the point of view of the system operation. A resistor of 0.5 Ω is connected between the inverters and the amplifier to model the battery's internal resistance. In order to provide an isolated voltage supply, the four-quadrant amplifier is supplied by an isolation transformer and is equipped with a resistor bank (RL 4000) to be able to sink the power during charging mode. The control algorithm is implemented in a dSPACE ds1006 control board, which supplies the inverters with gating signals. The dc-bus voltage, grid voltages, and the motor phase currents are measured with external Hall sensors, not shown in Fig. 8, and the signals are fed back to the control board.

The grid phase voltages are 240 V rms, 50 Hz. The inverters are switched at 10-kHz switching frequency, with asymmetrical PWM [22], so that the sampling frequency of 20 kHz is used. The dead time is 6 μs. The nine-phase induction machine parameters and data are given in Appendix B.

A. Charging Mode

The charging and V2G modes of operation are performed in the CC regime, in which the grid current magnitude is regulated to a constant value. The reference current is $i^*_{dg} = 4$ A, which corresponds to 1.73 smaller rms value of the phase currents (2.3 A), due to the power-invariant three-phase decoupling transformation on the grid side. The dc-bus voltage is set to 720 V for the charging and V2G operation.

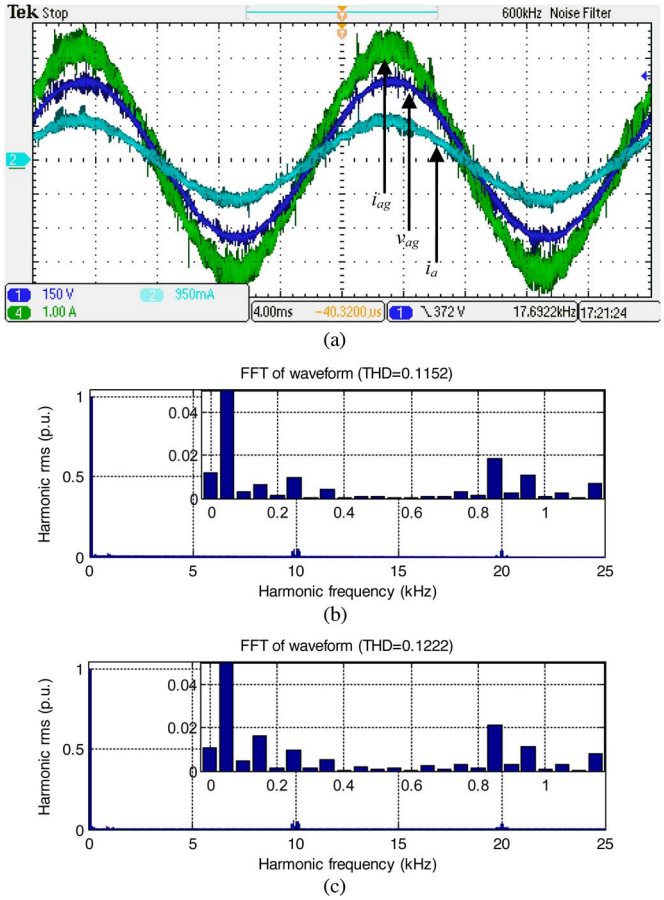

Fig. 9. Oscilloscope recordings and FFTs of measured variables for charging mode. (a) CH1—grid phase voltage v_{ag} (150 V/div), CH4—grid phase current i_{ag} (1 A/div), and CH2—machine phase current i_a (1 A/div) waveforms. (b) Grid phase current spectrum. (c) Machine phase current spectrum.

Fig. 9(a) shows the grid phase voltage, grid phase current, and machine's phase current. As can be seen, the fundamental of the grid current and phase voltage are in phase so that the operation is with unity power factor at the grid side. The fast Fourier transforms (FFTs) of the grid and machine phase currents are shown in Fig. 9(b) and (c), respectively.

The amplitude of the current ripple is dependent on the machine's stator leakage inductance (25 mH per phase here) since it performs the function of the current filter (due to the three phases being effectively paralleled, the equivalent filter inductance in the sense of Fig. 2 is $25/3 = 8.33$ mH). The grid current is the sum of the three phase currents in the machine, which are very similar to each other. Therefore, the grid current is three times higher than the machine's phase current (rms values of 2.3 and 0.8 A, respectively), and the grid current and machine current have very similar spectrum. The low-order harmonics are small; the highest ones reach around 1% of the fundamental. This is considered to be a good result, taking into account the high switching period/dead time ratio. It should be noted that harmonics above the 15th are not controlled. This is an arbitrary choice here, and the order of the harmonics that are controlled can be easily increased by adding further resonant VPI current controllers in parallel to those used here, shown in Fig. 5.

The grid current components i_{dg} and i_{qg} in the grid voltage-oriented reference frame are depicted in Fig. 10. The q-axis

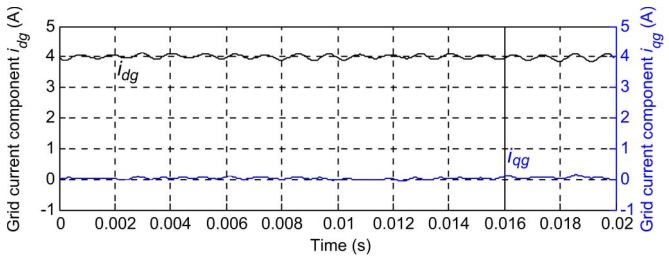

Fig. 10. Grid current components i_{dg} and i_{qg}, in charging mode, obtained within the controller after grid current transformation into voltage-oriented reference frame.

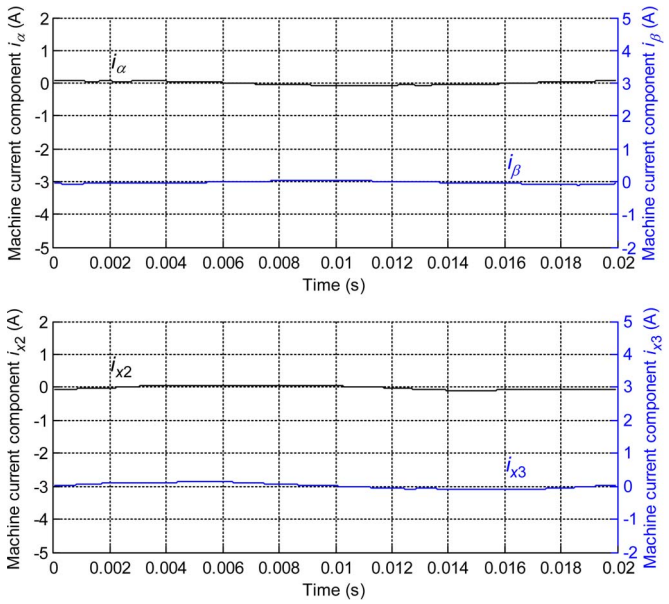

Fig. 11. Machine current components in inactive planes (i_α, i_β, i_{x2}, and i_{x3}), obtained within the controller after the machine's measured phase currents are transformed using (A.1).

component reference is fixed to zero, and the battery is charged with the d-axis component. Both components follow their references very well. Since the control operates in the grid-oriented reference frame and the average value of the q-axis current component is zero, Fig. 10 also confirms that the charging takes place at unity power factor.

The mapping of the machine phase currents into inactive planes is illustrated in Fig. 11, where i_α, i_β, i_{x2}, and i_{x3} are shown. There is a negligible excitation in any of these three planes. According to (4) and (5), the nonzero current components are in the first $x-y$ plane and along the zero-sequence axis. This is indeed the case, as is obvious from Fig. 12, where i_{x1}, i_{y1}, and i_0 are presented. There is also an asymmetrical distribution of the components in the x_1-y_1 plane [see (4)] as is evident in Fig. 12.

The battery charging current i_L is shown in Fig. 13. It can be seen that it is practically constant, about 2.13 A, with hardly any ripple. The speed trace is also included in Fig. 13—as can be seen, the speed is kept at zero naturally, meaning that there is no torque developed; this is also evident from Fig. 11, where $\alpha-\beta$ current components have zero value throughout.

As discussed in Section III-A, the control algorithm for the charging and V2G modes is based on the assumption that three phases of any of the three three-phase windings have identical

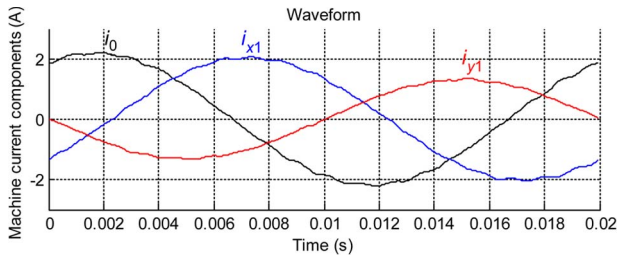

Fig. 12. Charging mode: Waveforms of the machine current components i_{x1}, i_{y1}, and i_0, obtained within the controller after the machine's measured phase currents are transformed using (A.1).

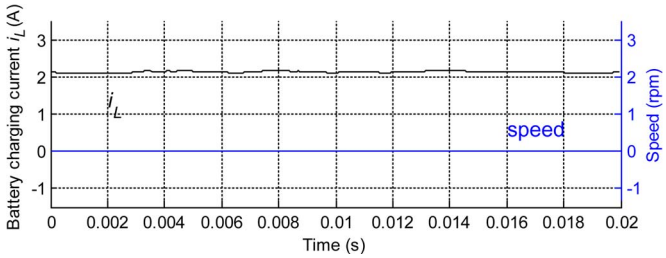

Fig. 13. Battery current i_L and machine's speed during charging.

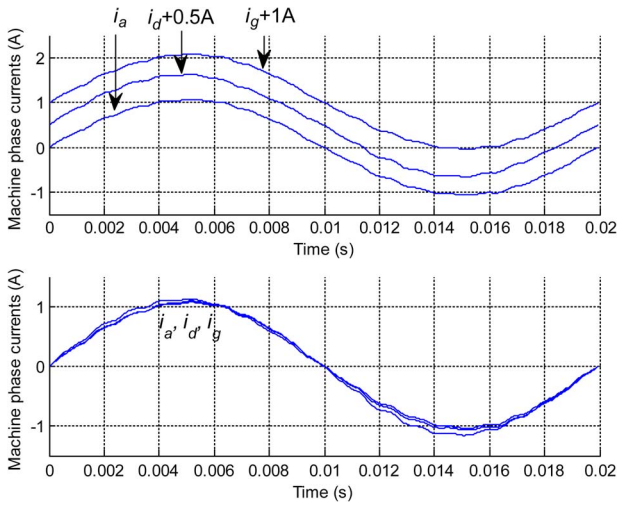

Fig. 14. Currents of one three-phase winding of the machine during charging process.

parameters, leading to the equal distribution of one grid phase current into three currents of the machine. To prove that this is indeed the case here, Fig. 14 shows the currents of the three phases of one three-phase winding during charging, for the operating conditions described earlier.

B. V2G Mode

By setting the reference grid d-axis current to a negative value, the power flow direction reverses, and the V2G mode is entered. Fig. 15 shows the grid phase voltage, grid phase current, and machine phase current waveforms (with FFTs of the grid and machine phase currents) for this mode of operation. Results apply to the reference current $i_{dg}^* = -3$ A.

The grid and machine current rms values are 1.73 and 0.6 A, respectively. The grid currents are in phase opposition with the grid voltage, which confirms the opposite power flow direction, compared to the charging mode, as well as the unity power

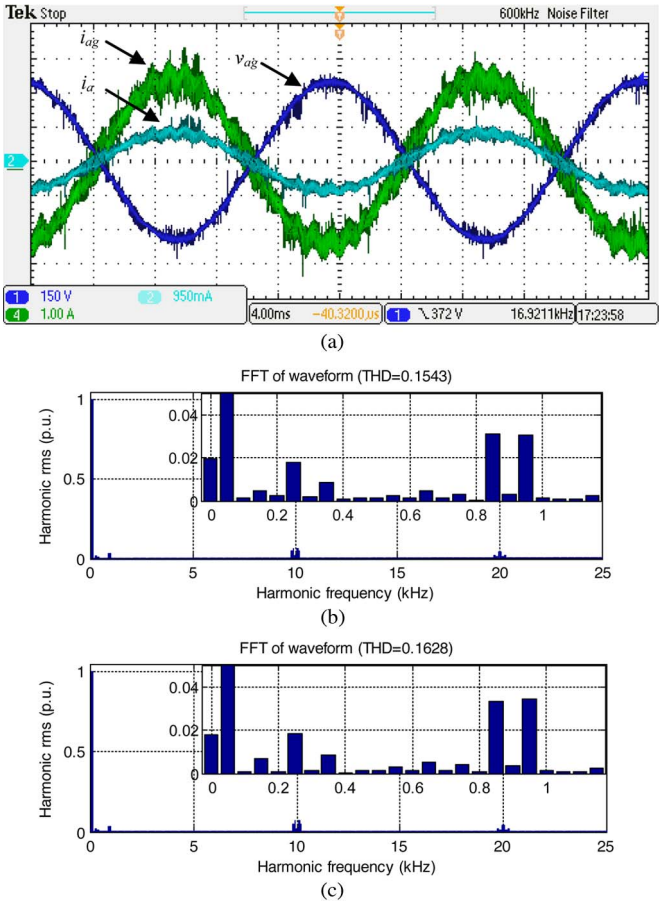

Fig. 15. Oscilloscope recordings and FFTs of measured variables for V2G mode. (a) CH1—grid phase voltage v_{ag} (150 V/div), CH4—grid phase current i_{ag} (1 A/div), and CH2—machine phase current i_a (1 A/div) waveforms. (b) Grid phase current spectrum. (c) Machine phase current spectrum.

factor operation. The amplitudes of the two currents are again in the ratio of 3, and the FFTs are similar. The low-order harmonics have slightly larger magnitudes in V2G than in the charging mode.

The comparison of the oscilloscope recordings of the grid currents in the charging and V2G modes, given in Figs. 9 and 15, respectively, shows similar gird current ripple. Harmonic per-unit values, given in Figs. 9 and 15, are, however, different, primarily because the fundamental grid current differs in the two modes. Using the fundamental grid current rms values of 2.3 and 1.73 A for the charging and V2G modes, respectively, and the grid current total harmonic distortion values given in Figs. 9(b) and 15(b), it is easy to establish that the current ripple rms values come in both modes to essentially the same value (0.265 and 0.267 A, respectively).

The grid current components i_{dg} and i_{qg} for the V2G mode are presented in Fig. 16. Once again, the reference currents are realized, and the unity power factor operation is reconfirmed.

The mapping of the machine currents into the planes is the same as in the charging mode. Currents i_α, i_β, i_{x2}, and i_{x3} are, in essence, zero since the grid currents in the machine map into i_0, i_{x1}, and i_{y1} currents (see Fig. 17). If compared with Fig. 12, it can be seen that they have opposite signs. The results are in accordance with (7) and (8).

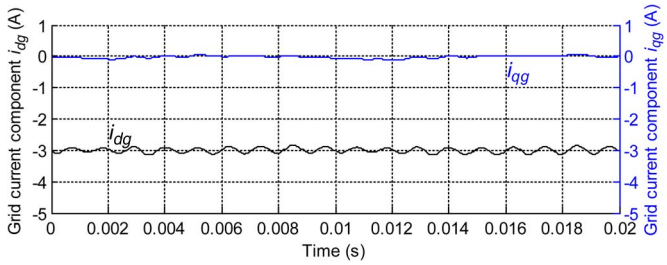

Fig. 16. Grid current components i_{dg} and i_{qg}, in V2G mode, obtained within the controller after grid current transformation into voltage-oriented reference frame.

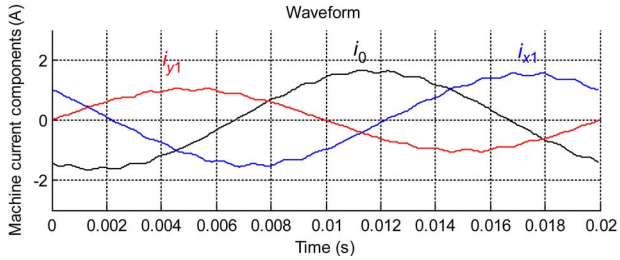

Fig. 17. V2G mode: Waveforms of the machine current components i_{x1}, i_{y1}, and i_0, obtained within the controller after the machine's measured phase currents are transformed using (A.1).

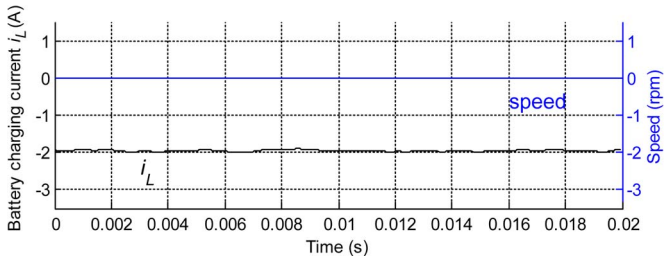

Fig. 18. Battery current i_L and machine's speed during V2G operation.

The battery charging current i_L is given in Fig. 18. It again has a constant value, around -1.95 A. Although the grid current amplitude is reduced by approximately 25% (compared to the charging mode), the battery current i_L changes much less. This is explained by the fact that, in the V2G mode, the battery has to produce the power for RI^2 losses in the filter (i.e., the machine) in addition to the power that is injected into the grid. On the other hand, in the charging mode, the battery charging power is what is left from the grid power after the filter losses are covered. In the V2G mode, the speed of the machine is again kept at zero, as can be seen in Fig. 18.

The transition from the V2G to the charging mode is illustrated next. The waveforms of the grid voltage, grid phase current, and battery current are shown in Fig. 19, while Fig. 20 shows the grid current components i_{dg} and i_{qg}. The transition is from $i_{dg}^* = -4$ A to $i_{dg}^* = 4$ A. Both figures indicate a fast transition between these two reference values. However, the VPI controllers need more time to eliminate the harmonics from the current waveform. From Fig. 19, it can be seen that, although grid currents have the same amplitudes for the two modes of operation, the battery charging current i_L is higher by absolute value for the V2G mode than for the charging mode, for the reason already discussed in the previous paragraph.

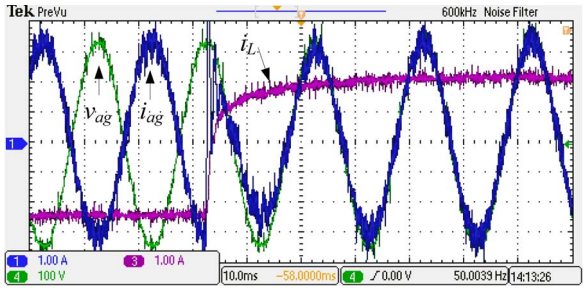

Fig. 19. Transient operation: CH4—grid phase voltage v_{ag} (100 V/div), CH3—dc-bus current i_{dc} (1 A/div), and CH1—grid phase current i_{ag} (1 A/div) waveforms for transition from V2G to charging mode (oscilloscope recordings).

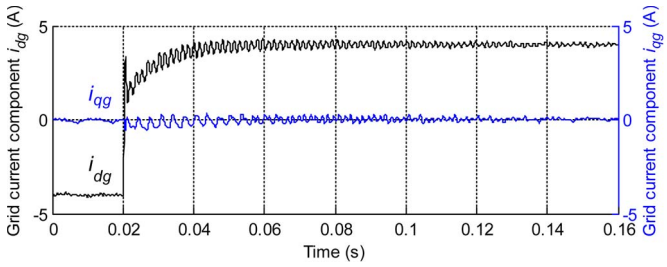

Fig. 20. Grid current components i_{dg} and i_{qg}, during transition from V2G into charging mode, obtained within the controller after grid current transformation into voltage-oriented reference frame.

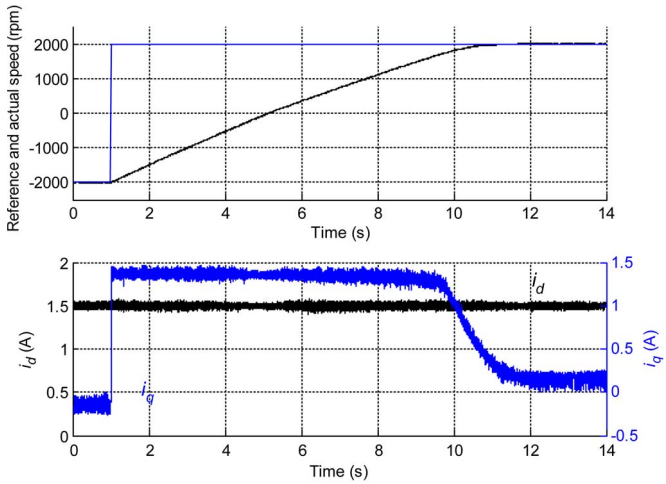

Fig. 21. Reference and actual rotor speed and machine current components i_d and i_q in propulsion mode: Reversal from −2000 to 2000 r/min.

C. Propulsion

The grid connections were removed to test the propulsion mode. Since a dc–dc converter will typically exist between the battery and the inverter, a different value of 600 V is used for the dc-bus voltage. The control algorithm of Section III-B is implemented in the dSPACE in order to verify that the machine works well in the propulsion regime. Figs. 21 and 22 show the obtained experimental results. A reversal transient, from −2000 to 2000 r/min, is examined, with the rotor position information provided by an encoder.

Fig. 21 shows the machine reference and actual speed waveforms and machine current components i_d and i_q. The reference value for the i_d current is 1.5 A, and the i_q current was limited to 1.4 A [the corresponding rms phase current values are three

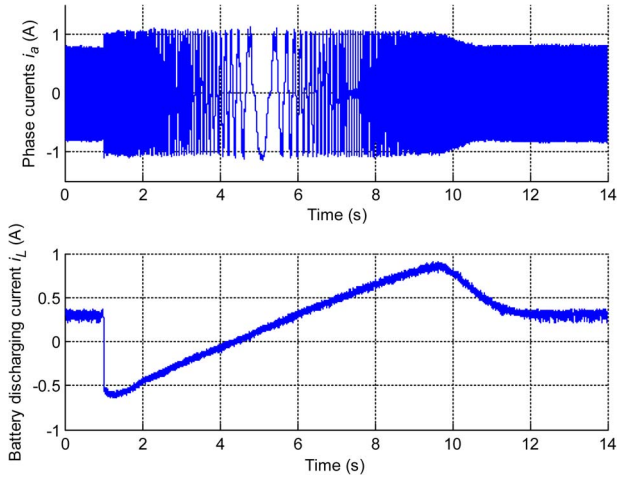

Fig. 22. Motor phase current and current taken from the battery in propulsion mode: Reversal from −2000 to 2000 r/min.

times smaller, due to the use of (A.2)]. The reversal transient has been made deliberately slow, by using a low limit on the stator q-axis current reference. Fig. 22 shows the phase current and dc-bus current during the same transient.

One interesting feature of the system is that the energy released during electric braking is automatically used to recharge the battery. This is evident in the trace of the dc-bus current in the beginning of the transient, when the current is negative. Figs. 21 and 22 demonstrate excellent performance in the propulsion mode, as is to be expected from rotor flux oriented control.

As mentioned in Section II, one advantage of multiphase machines over their three-phase counterparts is that the additional degrees of freedom enable relatively easy fault-tolerant control. This applies to open-phase faults, where the loss of one or more phases can be tolerated by an appropriate control algorithm reconfiguration so that the machine continues to operate with rotating field and smooth but reduced torque output. Since EVs are torque drives, a reduction in torque simply transfers into a reduction of speed, which is perfectly acceptable for the "limp home" mode. A detailed discussion of the control algorithms for fault-tolerant operation is beyond the scope of this paper, but it has been treated in numerous papers for specific phase numbers (see, for example, [23] for a detailed study of fault-tolerant control for an asymmetrical six-phase induction machine with single and two isolated neutral points). It suffices here to say that the simplest fault-tolerant mode results by taking out of service a complete three-phase winding in which an open-phase fault has taken place. This means that the machine would be able to continue operation with the rotating field and smooth (but reduced) torque as long as at least one three-phase winding has all three healthy phases.

V. Conclusion

This paper has introduced a novel solution for the fast integrated onboard charging of EVs. The proposed configuration is based on the application of an asymmetrical nine-phase machine. It has the advantages of unity power factor operation and zero average torque production in the machine during the charging mode. Moreover, no hardware reconfiguration is required between the propulsion and charging/V2G modes of

$$[C]=\sqrt{\frac{2}{9}}\begin{array}{c}\\ \alpha\\ \beta\\ x_1\\ y_1\\ x_2\\ y_2\\ x_3\\ y_3\\ 0\end{array}\begin{array}{c}\begin{array}{ccccccccc} a & b & c & d & e & f & g & h & i\end{array}\\ \begin{bmatrix} 1 & \cos(\alpha) & \cos(2\alpha) & \cos(6\alpha) & \cos(7\alpha) & \cos(8\alpha) & \cos(12\alpha) & \cos(13\alpha) & \cos(14\alpha)\\ 0 & \sin(\alpha) & \sin(2\alpha) & \sin(6\alpha) & \sin(7\alpha) & \sin(8\alpha) & \sin(12\alpha) & \sin(13\alpha) & \sin(14\alpha)\\ 1 & \cos(3\alpha) & \cos(6\alpha) & 1 & \cos(3\alpha) & \cos(6\alpha) & 1 & \cos(3\alpha) & \cos(6\alpha)\\ 0 & \sin(3\alpha) & \sin(6\alpha) & 0 & \sin(3\alpha) & \sin(6\alpha) & 0 & \sin(3\alpha) & \sin(6\alpha)\\ 1 & \cos(5\alpha) & \cos(10\alpha) & \cos(12\alpha) & \cos(17\alpha) & \cos(4\alpha) & \cos(6\alpha) & \cos(11\alpha) & \cos(16\alpha)\\ 0 & \sin(5\alpha) & \sin(10\alpha) & \sin(12\alpha) & \sin(17\alpha) & \sin(4\alpha) & \sin(6\alpha) & \sin(11\alpha) & \sin(16\alpha)\\ 1 & \cos(7\alpha) & \cos(14\alpha) & \cos(6\alpha) & \cos(13\alpha) & \cos(2\alpha) & \cos(12\alpha) & \cos(\alpha) & \cos(8\alpha)\\ 0 & \sin(7\alpha) & \sin(14\alpha) & \sin(6\alpha) & \sin(13\alpha) & \sin(2\alpha) & \sin(12\alpha) & \sin(\alpha) & \sin(8\alpha)\\ 1/\sqrt{2} & -1/\sqrt{2} & 1/\sqrt{2} & 1/\sqrt{2} & -1/\sqrt{2} & 1/\sqrt{2} & 1/\sqrt{2} & -1/\sqrt{2} & 1/\sqrt{2}\end{bmatrix}\end{array} \tag{A.1}$$

$$[C]=\sqrt{\frac{2}{9}}\begin{array}{c}\\ \alpha\\ \beta\\ x_1\\ y_1\\ x_2\\ y_2\\ 0_1\\ 0_2\\ 0_3\end{array}\begin{array}{c}\begin{array}{ccccccccc} a & b & c & d & e & f & g & h & i\end{array}\\ \begin{bmatrix} 1 & \cos(\alpha) & \cos(2\alpha) & \cos(6\alpha) & \cos(7\alpha) & \cos(8\alpha) & \cos(12\alpha) & \cos(13\alpha) & \cos(14\alpha)\\ 0 & \sin(\alpha) & \sin(2\alpha) & \sin(6\alpha) & \sin(7\alpha) & \sin(8\alpha) & \sin(12\alpha) & \sin(13\alpha) & \sin(14\alpha)\\ 1 & \cos(5\alpha) & \cos(10\alpha) & \cos(12\alpha) & \cos(17\alpha) & \cos(4\alpha) & \cos(6\alpha) & \cos(11\alpha) & \cos(16\alpha)\\ 0 & \sin(5\alpha) & \sin(10\alpha) & \sin(12\alpha) & \sin(17\alpha) & \sin(4\alpha) & \sin(6\alpha) & \sin(11\alpha) & \sin(16\alpha)\\ 1 & \cos(7\alpha) & \cos(14\alpha) & \cos(6\alpha) & \cos(13\alpha) & \cos(2\alpha) & \cos(12\alpha) & \cos(\alpha) & \cos(8\alpha)\\ 0 & \sin(7\alpha) & \sin(14\alpha) & \sin(6\alpha) & \sin(13\alpha) & \sin(2\alpha) & \sin(12\alpha) & \sin(\alpha) & \sin(8\alpha)\\ \sqrt{3/2} & 0 & 0 & \sqrt{3/2} & 0 & 0 & \sqrt{3/2} & 0 & 0\\ 0 & \sqrt{3/2} & 0 & 0 & \sqrt{3/2} & 0 & 0 & \sqrt{3/2} & 0\\ 0 & 0 & \sqrt{3/2} & 0 & 0 & \sqrt{3/2} & 0 & 0 & \sqrt{3/2}\end{bmatrix}\end{array} \tag{A.2}$$

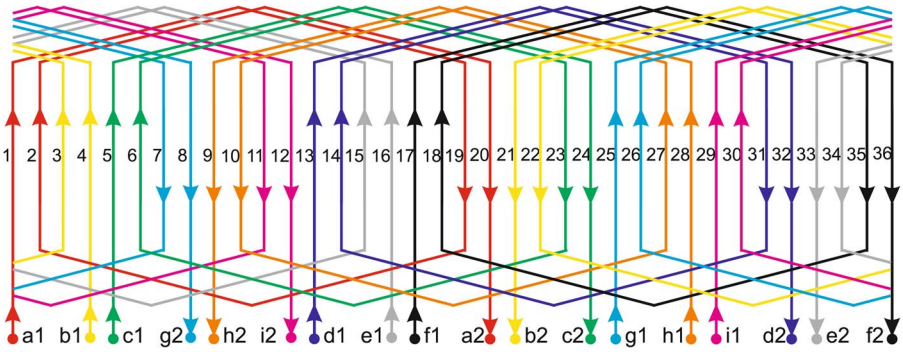

Fig. 23. Stator winding layout of the asymmetrical nine-phase machine (numbers 1 and 2 denote beginnings and endings of the phases).

operation. Stator leakage inductances of the machine are used to ensure filtering during the charging/V2G operation. The theoretical viability of charging/V2G without torque production is examined, and control algorithms for the charging, V2G, and propulsion modes of operation are given. The presented control scheme is well suited to the situation in which there are no asymmetries within each individual three-phase winding. If this is not the case, an additional current balancing control algorithm would be required in practice. Theoretical results are validated by experiments.

Appendix A
Transformation Matrices

The nine-phase machine is regarded as having a near-sinusoidal magnetomotive force distribution. According to Fig. 1, during the charging and V2G operation, the machine is in the open-end winding configuration, and each three-phase set of the nine-phase machine is connected to one phase of the grid (i.e., paralleled to it, as indicated in Fig. 2). Hence, the behavior of the nine-phase system is governed by the single neutral point, at the three-phase grid side. The decoupling transformation matrix for an asymmetrical nine-phase system with a single neutral point is, according to [14] and taking into account that $\alpha = 20°$, given with (A.1), shown at the top of the page.

In the propulsion mode, the grid is disconnected. Hence, the three neutral points of the nine-phase winding are floating, and the system behaves as having three isolated neutral points. The decoupling transformation matrix for an asymmetrical nine-phase system with three isolated neutral points is governed with (A.2), shown at the top of the page.

Appendix B
Machine and Other Data

DC sink/source: "Spitzenberger & Spies"—two DM 2500/PAS single-phase mains emulation systems are connected in series. Each provides half of the dc-bus voltage. An additional resistive load (RL 4000) is connected to the supply, enabling power sinking of up to 4 kW.

Controller: dSPACE DS1006 processor board. A DS2004 high-speed A/D board is used for the A/D conversion of the measured machine phase currents and grid voltages. A DS5101 digital waveform output board is used for the

PWM signal generation, and the machine speed is read by a DS3002 incremental encoder interface board.

Converters: Two two-level eight-phase inverters. The insulated gate bipolar transistors used are EUPEC FS50R12KE3. Using the heat-sink data, it is estimated that the rated continuous output rms current is 14 A, which gives the overall nine-phase inverter continuous rating of approximately 32 kVA for a 240-V rms phase voltage.

Asymmetrical nine-phase machine: The machine was obtained by rewinding the stator of a three-phase machine with rated data 2.2 kW, 230 V (phase-to-neutral), 50 Hz, 4.5 A, $\cos\phi = 0.83$, two pole pairs, and 36 stator slots. After rewinding, the nine-phase machine is 2.2 kW, 230 V (phase-to-neutral), 50 Hz, and 1.5 A, with one pole pair. The winding layout is shown in Fig. 23.

The equivalent circuit parameters of the nine-phase machine are as follows: $R_s = 6.5\,\Omega$, $R_r = 1.3\,\Omega$, $L_{\gamma s} = 25$ mH, $L_{\gamma r} = 9$ mH, $L_m = 1.3$ H.

REFERENCES

[1] J. M. Slicker, "Pulse width modulation inverter with battery charger," U.S. Patent 4 491 768, Jan. 1, 1985.

[2] S. Haghbin, S. Lundmark, M. Alakula, and O. Carlson, "Grid-connected integrated battery chargers in vehicle applications: Review and new solution," *IEEE Trans. Ind. Electron.*, vol. 60, no. 2, pp. 459–473, Feb. 2013.

[3] J. D. Santiago *et al.*, "Electrical motor drivelines in commercial all-electric vehicles: A review," *IEEE Trans. Veh. Technol.*, vol. 61, no. 2, pp. 475–484, Feb. 2012.

[4] S. Kinoshita, "Electric system of electric vehicle," U.S. Patent 5 629 603, May 13, 1997.

[5] F. Lacressonniere and B. Cassoret, "Converter used as a battery charger and a motor speed controller in an industrial truck," in *Proc. EPE. Appl. Conf.*, Dresden, Germany, 2005, pp. 1–7.

[6] S. Haghbin, S. Lundmark, M. Alakula, and O. Carlson, "An isolated high-power integrated charger in electrified-vehicle applications," *IEEE Trans. Veh. Technol.*, vol. 60, no. 9, pp. 4115–4126, Nov. 2011.

[7] I. Subotic, E. Levi, M. Jones, and D. Graovac, "Multiphase integrated on-board battery chargers for electrical vehicles," in *Proc. EPE Appl. Conf.*, Lille, France, 2013, pp. 1–10.

[8] L. De Sousa, B. Silvestre, and B. Bouchez, "A combined multiphase electric drive and fast battery charger for electric vehicles," in *Proc. IEEE VPPC*, Lille, France, 2010, pp. 1–6.

[9] Renault press kit Renault ZOE: The electric supermini for everyday use, Feb. 26, 2013. [Online]. Available: www.media.renault.com, Renault press kit

[10] I. Subotic, E. Levi, M. Jones, and D. Graovac, "An integrated battery charger for EVs based on an asymmetrical six-phase machine," in *Proc. IEEE IECON*, Vienna, Austria, 2013, pp. 7242–7247.

[11] I. Subotic, E. Levi, M. Jones, and D. Graovac, "On-board integrated battery chargers for electric vehicles using nine-phase machines," in *Proc. IEEE IEMDC*, Chicago, IL, USA, 2013, pp. 239–246.

[12] A. P. Sandulescu, F. Meinguet, X. Kestelyn, E. Semail, and A. Bruyere, "Flux-weakening operation of open-end winding drive integrating a cost-effective high-power charger," *IET Elect. Syst. Transp.*, vol. 3, no. 1, pp. 10–21, Mar. 2013.

[13] E. Levi, M. Jones, S. N. Vukosavic, and H. A. Toliyat, "A novel concept of a multiphase, multimotor vector controlled drive system supplied from a single voltage source inverter," *IEEE Trans. Power Electron.*, vol. 19, no. 2, pp. 320–335, Mar. 2004.

[14] A. A. Rockhill and T. A. Lipo, "A simplified model of a nine-phase synchronous machine using vector space decomposition," *Elect. Power Compon. Syst.*, vol. 38, no. 4, pp. 477–489, Jan. 2010.

[15] E. Levi, R. Bojoi, F. Profumo, H. A. Toliyat, and S. Williamson, "Multiphase induction motor drives—A technology status review," *IET Elect. Power Appl.*, vol. 1, no. 4, pp. 489–516, Jul. 2007.

[16] L. R. Limongi, R. Bojoi, C. Pica, F. Profumo, and A. Tenconi, "Analysis and comparison of phase locked loop techniques for grid utility applications," in *Proc. PCC*, Nagoya, Japan, 2007, pp. 674–681.

[17] S. Dusmez, A. Cook, and A. Khaligh, "Comprehensive analysis of high quality power converters for level 3 off-board chargers," in *Proc. IEEE VPPC*, Chicago, IL, USA, 2011, pp. 674–681.

[18] A. G. Yepes, "Digital resonant current controllers for voltage source converters," Ph.D. dissertation, Univ. Vigo, Vigo, Spain, 2011.

[19] C. Lascu, L. Asiminoaei, I. Boldea, and F. Blaabjerg, "High performance current controller for selective harmonic compensation in active power filters," *IEEE Trans. Power Electron.*, vol. 22, no. 5, pp. 1826–1835, Sep. 2007.

[20] E. Levi, "FOC: Field oriented control," in *The Industrial Electronics Handbook—Power Electronics and Motor Drives (Chapter 24)*, B. M. Willamowski and J. D. Irwin, Eds. Boca Raton, FL, USA: CRC Press, 2011.

[21] H. S. Che, E. Levi, M. Jones, W. P. Hew, and N. A. Rahim, "Current control methods for an asymmetrical six-phase induction motor drive," *IEEE Trans. Power Electron.*, vol. 29, no. 1, pp. 407–417, Jan. 2014.

[22] D.G. Holmes and T.A. Lipo, *Pulse Width Modulation for Power Converters: Principles and Practice*. Piscataway, NJ, USA: IEEE Press, 2003.

[23] H. S. Che *et al.*, "Post-fault operation of an asymmetrical six-phase induction machine with single and two isolated neutral points," *IEEE Trans. Power Electron.*, vol. 29, no. 10, pp. 5406–5416, Oct. 2014.

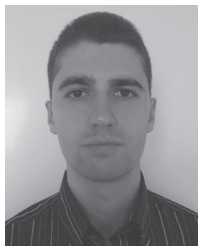

Ivan Subotic (S'12) received the Dipl. Ing. and M.Sc. degrees in electrical engineering from the University of Belgrade, Belgrade, Serbia, in 2010 and 2011, respectively. He has been working toward the Ph.D. degree at Liverpool John Moores University, Liverpool, U.K., since 2011.

His main research interests include power electronics, electric vehicles, and control of multiphase drive systems.

Nandor Bodo received the M.S. degree in power electronics from the University of Novi Sad, Novi Sad, Serbia, in 2009 and the Ph.D. degree in electrical engineering from Liverpool John Moores University, Liverpool, U.K., in 2013.

He is currently with Liverpool John Moores University as a Postdoctoral Research Associate. His research interests include power electronics and variable-speed drives.

Emil Levi (S'89–M'92–SM'99–F'09) received the M.Sc. and Ph.D. degrees in electrical engineering from the University of Belgrade, Belgrade, Serbia, in 1986 and 1990, respectively.

From 1982 to 1992, he was with the Department of Electrical Engineering, University of Novi Sad, Novi Sad, Serbia. He joined Liverpool John Moores University, Liverpool, U.K., in May 1992 and has been a Professor of Electric Machines and Drives since September 2000.

Dr. Levi served as a Coeditor-in-Chief of the IEEE TRANSACTIONS ON INDUSTRIAL ELECTRONICS during 2009–2013 and is currently the Editor-in-Chief of *IET Electric Power Applications* and an Editor of the IEEE TRANSACTIONS ON ENERGY CONVERSION. He was the recipient of the Cyril Veinott Award of the IEEE Power and Energy Society in 2009 and the Best Paper Award of the IEEE TRANSACTIONS ON INDUSTRIAL ELECTRONICS in 2008.

Martin Jones received the B.Eng. degree (first-class honors) in electrical engineering from Liverpool John Moores University, Liverpool, U.K., in 2001. He was a research student at Liverpool John Moores University from September 2001 to Spring 2005, when he received his Ph.D. degree in electrical engineering.

He is currently with Liverpool John Moores University as a Reader. His research is in the area of high-performance ac drives.

Dr. Jones was a recipient of the IEE Robinson Research Scholarship for his Ph.D. studies.